Received: 14 March 2023 | Revised: 11 July 2024 | Accepted: 20 July 2024

DOI: 10.1111/ejn.16490

RESEARCH REPORT

EJN European Journal of Neuroscience FENS WILEY

Comparison of T1-weighted landmark placement and ROI transfer onto diffusion-weighted EPI sequences for targeted tractography tasks in the optic nerve

Markus Janko[1] | **Sascha D. Santaniello**[1] | **Carolin Brockmann**[1] | **Marcel Wolf**[1] | **Nils F. Grauhan**[1] | **Vanessa I. Schöffling**[1] | **Violeta Dimova**[2] | **Katharina Ponto**[3] | **Esther M. Hoffmann**[3] | **Wolfgang Kleinekofort**[4] | **Ahmed E. Othman**[1] | **Marc A. Brockmann**[1] | **Andrea Kronfeld**[1]

[1]Department of Neuroradiology, University Medical Center of the Johannes Gutenberg-University Mainz, Mainz, Germany

[2]Department of Neurology, University Medical Center of the Johannes Gutenberg-University Mainz, Mainz, Germany

[3]Department of Ophthalmology, University Medical Center of the Johannes Gutenberg-University Mainz, Mainz, Germany

[4]Applied Physics & Medical Engineering, Hochschule RheinMain, Rüsselsheim, Germany

Correspondence
Markus Janko, Department of Neuroradiology, University Medical Center of the Johannes Gutenberg-University of Mainz, Langenbeckstraße 1, 55131 Mainz, Germany.
Email: mrksjanko@gmail.com

Funding information
This research did not receive any specific grant from funding agencies in the public, commercial, or not-for-profit sectors.

Abstract

Diffusion-based tractography in the optic nerve requires sampling strategies assisted by anatomical landmark information (regions of interest [ROIs]). We aimed to investigate the feasibility of expert-placed, high-resolution T1-weighted ROI-data transfer onto lower spatial resolution diffusion-weighted images.

Slab volumes from 20 volunteers were acquired and preprocessed including distortion bias correction and artifact reduction. Constrained spherical deconvolution was used to generate a directional diffusion information grid (fibre orientation distribution-model [FOD]). Three neuroradiologists marked landmarks on both diffusion imaging variants and structural datasets. Structural ROI information (volumetric interpolated breath-hold sequence [VIBE]) was respectively registered (linear with 6/12 degrees of freedom [DOF]) onto single-shot EPI (ss-EPI) and readout-segmented EPI (rs-EPI) volumes, respectively. All eight ROI/FOD-combinations were compared in a targeted tractography task of the optic nerve pathway.

Inter-rater reliability for placed ROIs among experts was highest in VIBE images (lower confidence interval 0.84 to 0.97, mean 0.91) and lower in both ss-EPI (0.61 to 0.95, mean 0.79) and rs-EPI (0.59 to 0.86, mean 0.70).

Tractography success rate based on streamline selection performance was highest in VIBE-drawn ROIs registered (6-DOF) onto rs-EPI FOD (70.0% over

Abbreviations: CI, confidence interval; CSD, constrained spherical convolution; DOF, degree of freedom; DWI, diffusion-weighted (magnetic resonance) imaging; EPI, echo-planar imaging; FLIRT, FMRIB's Linear Image Registration Tool; FOD, fibre orientation distribution; FOV, field of view; HARDI, high-angular-resolution diffusion-weighted imaging; ICC, intraclass correlation coefficient; MR, magnetic resonance; OC, optic chiasm; ON, optic nerve; ONH, optic nerve head; ROI, region of interest; rs-EPI, readout-segmented EPI; SMS, simultaneous multi-slice; ss-EPI, single-shot EPI; VIBE, volumetric interpolated breath-hold sequence; WM, white matter.

Edited by: John Foxe

5%-threshold, capped to failed ratio 39/16) followed by both 12-DOF-registered (67.5%; 41/16) and nonregistered VIBE (67.5%; 40/23). On ss-EPI FOD, VIBE-ROI-datasets obtained fewer streamlines overall with each at 55.0% above 5%-threshold and with lower capped to failed ratio (6-DOF: 35/36; 12-DOF: 34/34, nonregistered 33/36).

The combination of VIBE-placed ROIs (highest inter-rater reliability) with 6-DOF registration onto rs-EPI targets (best streamline selection performance) is most suitable for white matter template generation required in group studies.

KEYWORDS

diffusion-weighted imaging, magnetic resonance imaging, optic nerve, preprocessing, registration, tractography, white matter templates

1 | INTRODUCTION

Optic nerve (ON) pathologies and the associated compromised vision cause a significant decline in quality of life (Wu, 2019). Deterioration of the nerve fibres themselves or malignant impairment of their integrity, form or pathway (e.g., caused by tumour growth) can, if undetected and untreated, result in a complete vision loss (Becker et al., 2010). Classical noninvasive diagnostic ophthalmologic methods (slit lamp-assisted ophthalmoscopy, diagnostic laser-based imaging such as optical coherence tomography) for the assessment of the optic nerve head (ONH, *papilla*) approach the ocular globe through the pupil, the lens and its translucent main body (*corpus vitreum*) (Weinreb et al., 2014). In clinical practice, ONH morphology provides information on disease progression, particularly in glaucoma (Weinreb et al., 2014). However, these methods are unable to depict the deeper portions of the ON due to their limited depth of penetration (Altıntaş et al., 2017; Sims et al., 2020).

The use of diffusion-weighted magnetic resonance (MR) imaging (DWI (Le Bihan & Breton, 1985)) in combination with nerve fibre tracking methods (tractography (Basser et al., 2000)) provides additional tools (Brockmann & Elflein, 2019; Mori & Zhang, 2006). DWI indirectly implicates the presence as well as the characteristic structure of nerve fibre pathways by measuring water molecule diffusion anisotropy (Sims et al., 2020). Tractography in neuroscience is generally utilized for the structural depiction of nerve fibre trajectories, and this information further applied into pre-surgical planning (Golby et al., 2011; Jacquesson et al., 2019) or to chart and analyze global (Sotiropoulos et al., 2013) or regional connectivity between segmented sub-areas of the brain (Nucifora et al., 2007). Beyond that, it can be used as a sampling strategy, in which diffusion-derived metrics along a selection of streamlines are analyzed (Riffert et al., 2014). Constrained spherical deconvolution (CSD) modelling techniques and their associated fibre orientation distribution-model (FOD) (Tournier et al., 2004, 2008) are state of the art in DWI tractography due to their potential for a better differentiation of diverging or crossing populations of white matter (WM) fibres (Raffelt et al., 2017) and have replaced preceding tensor-based models (Becker et al., 2020; Riffert et al., 2014).

In neuroimaging research, data evaluation makes use of standardized templates to save time, obtain more objective results or conduct group analyses. This is especially helpful in the analysis of data with low spatial resolution and/or low image quality such as DWI (Archer et al., 2018). In global (whole-brain) tractography, optimal templates completely cover WM and form a confined space in which streamlines are generated (seeded), proceeded and terminated exclusively (Christiaens et al., 2015; Mangin et al., 2013), thereby emulating biological reality. For analysis, tract bundle populations of interest are filtered out of the generated total afterwards.

Some areas of interest exclude the use of algorithmically generated WM templates, due to poor tissue differentiability in diffusion-weighted images (Chow & Paley, 2021). Regarding the ON pathway, this particularly concerns the intercranial part between optic canal and its partial decussation in the optic chiasm (OC) (Becker et al., 2010; Salazar et al., 2018) as a consequence of motion blurring, as well as susceptibility artifacts caused by varying magnetization characteristics in adjacent tissues (Andersson & Sotiropoulos, 2016; Le Bihan et al., 2006).

Strategies for compensation have either included template generation relying on manually drawn coverage of all assumed WM (He et al., 2020) or targeted

tractography. The latter technique utilizes manually placed regions of interest (ROIs), serving as mandatory spatial inclusion parameters for tractography algorithms. Approaches can be classified into those with multiple smaller ROIs (Haykal et al., 2020) and those with fewer and larger ROIs, resulting in oversampling that requires subsequent software-based and manual cleaning (pruning) steps (Allen et al., 2018; Miller et al., 2019). All non-automated ROI placement approaches are however highly susceptible to subjective variability in placement, with respect to both intra- and interindividual differences (Hakulinen et al., 2012; Suarez et al., 2012).

In this study, we have chosen an undersampling approach. Biases in ROI placement might be mitigable by transfer of anatomical landmark information (atlas-based or manually placed) from supplementary T1-weighted image acquisitions (3D volumetric interpolated breath-hold sequence [VIBE] (Rofsky et al., 1999)). For such purposes, a successful registration between structural images and target DWI volumes (Chen et al., 2019) and preliminary processing steps are necessary to adjust distortion in target DWI volumes and perform artifact reduction (Andersson et al., 2003).

Even though susceptibility variations along the ON pathway pose a challenge for echo-planar imaging (EPI) sequences, no practical alternative regarding acquisition speed in DWI exists so far (Wu & Miller, 2017). We therefore compared a standard single-shot EPI (ss-EPI) sequence to a readout-segmented EPI (rs-EPI) sequence contortion (RESOLVE, Siemens Healthineers, Germany), the latter applying a varied, less susceptibility-prone recording pattern, in addition to self-monitoring correction methods (Porter & Heidemann, 2009). Despite a raised overall acquisition time, RESOLVE enables a reduced distortion impact during imaging (Koyasu et al., 2014; Morelli et al., 2013; Yeom et al., 2013). Consequently, previous studies have shown superior results in the visual examination of parts of the ON, for example, in optical neuritis (Wan et al., 2016), in intraorbital ON image quality (Xu et al., 2016) and in intraorbital detection reliability and feasibility (Zhou et al., 2022) compared to ss-EPI.

This study aimed to compare methods of transferring expert-placed T1-weighted ON landmarks combined with preprocessing steps and registration strategies to optimize ROI position transfer between structural and diffusion-weighted images. Evaluation of successful streamline selection and variations across ROI, FOD and registration (via degrees of freedom [DOF]) combinations in a standardized targeted tracking task served as performance criteria. Informed selection of appropriate methodical combinations for further use in ON template-generation research serves as the purpose of our study.

2 | MATERIAL AND METHODS

2.1 | Acquisition

Imaging was performed using a 3.0 T MR scanner (Magnetom Skyra, Siemens, Germany) using a 64-channel head-coil. Twenty volunteers of age >18 years were included in this study (mean age 29.17 ± 5.34 SD, 5 females). Exclusion criteria have been (i) no ON-related pre-existing pathologies and (ii) three volunteers wearing prescription glasses with a diopter value of ±3 were checked individually for extreme anatomic distortions of the ON.

All participants underwent diffusion-weighted MRI using a ss-EPI and a rs-EPI (with three readout-direction segmentations) pulse sequence covering the optic tract (both 2.5 mm isometric voxels, four directions of $b = 0$, 30 directions of each $b = 800$ and 1600 s/mm^2, 16 slices, FOV = 220 mm). This resulted in an acquisition time of 3:02 min for ss-EPI and 10:27 min for rs-EPI, respectively. Opposed phase datasets were additionally acquired, consisting of 4 $b = 0$ images for each EPI variant (Andersson et al., 2003). Structural dataset acquisition followed EPI position and orientation, with higher resolution (VIBE, voxel size $1 \times 0.8 \times 0.8$ mm^3, TR 6.42 ms, TE 3.69 ms). Structural images obtained with VIBE sequences proved to be the most convenient for processing and for differentiating tissue types around the ON in preliminary experiments. The comparability of VIBE to other T1-weighted sequences has already been demonstrated by Wetzel et al., 2002.

To allow passing downwards along their body axis, the subjects' upward line of sight was diverted (90°) by an in-build head-coil mirror. A multi-coloured pictogram was used as a visual targeting point in order to avoid eye movement and consequential shifts of the ON. Individuals were instructed to maintain their visual focus in a relaxed manner and to avoid physical stress and exhaustion (Moodley et al., 2014).

2.2 | Preprocessing

To preprocess the datasets prior to FOD-generation and tractography, we opted into using an in-house rebuild of the TractoFlow pipeline (Theaud et al., 2020) and applied it on our acquired slabs. These slabs included the ocular globes, the osseous orbit and the intracranial part of the ON up to the OC, as well as coverage of the whole course of the optic tract and optic radiation up into the visual cortex.

MRtrix3 (Tournier et al., 2019), ANTS (Avants et al., 2014), FSL (Jenkinson et al., 2012) and scripts from the experimental Scilpy (Sherbrooke Connectivity Imaging Lab [Scilpy, 2021]/2015) python library were applied in accordance to their use in the TractoFlow pipeline.

The main technique for distortion correction (topup from the FSL package) employed supplementary DWI volumes with reversed acquisition direction (opposed phase) for calculating the influence of directional distortion-biases by cancelling them out (Andersson et al., 2003). Additional corrections, such as denoising or bias field correction, were deemed conservatively enough to avoid DWI-data falsification and derived from existing DWI preprocessing pipelines (Theaud et al., 2020).

All DWI datasets underwent the workflow shown in Figure 1, whilst omitting all steps from TractoFlow that concerned normalization and use of whole-brain templates for group studies. The supplementary structural VIBE datasets also underwent preprocessing according to the steps in the TractoFlow structural data preprocessing. After passing the pipeline, all image volumes were checked for successful completion.

2.3 | ROI placement

Three experienced neuroradiologists (readers: C.B. 18 years, M.W. 13 years and N.F.G. with 5 years of experience) placed ROIs in a scheme according to Haykal et al. (2020) in each structural image as well as in the diffusion datasets (see Figure 2). In order to standardize the

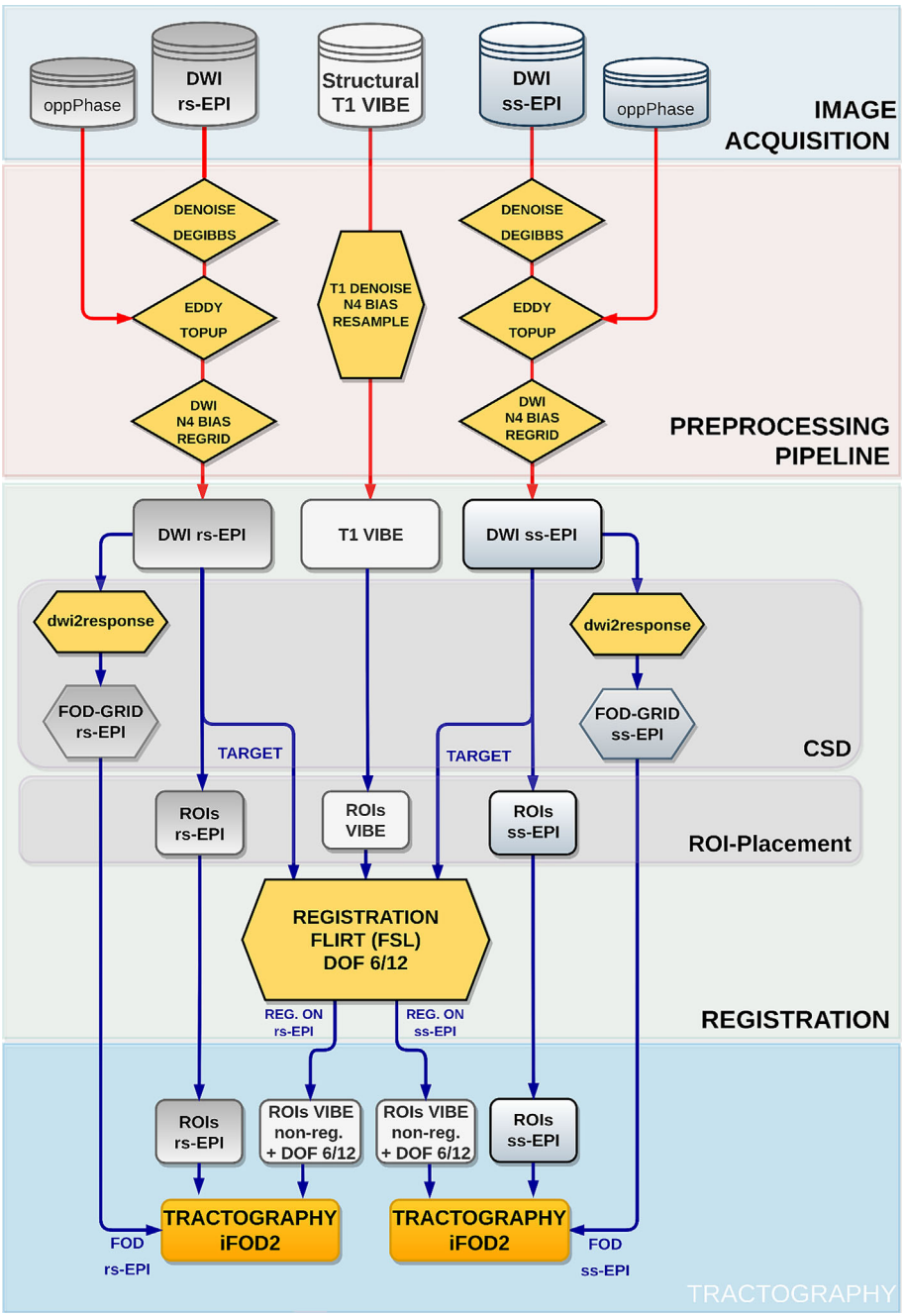

FIGURE 1 Complete project overview. Raw data in the image acquisition step is represented as stacks and continuously colour-coded in processed panel forms. Executed programmes during preprocessing steps are represented in yellow rhomboids. Prior to the registration of VIBE-drawn regions of interest (ROIs) onto respective diffusion-weighted magnetic resonance imaging (DWI)-variants, fibre orientation distribution (FOD) generation as well as ROI placement by expert readers takes place. Tractography algorithms are shown in orange and use combinations of either rs-/ss-FODs and (un)registered ROIs.

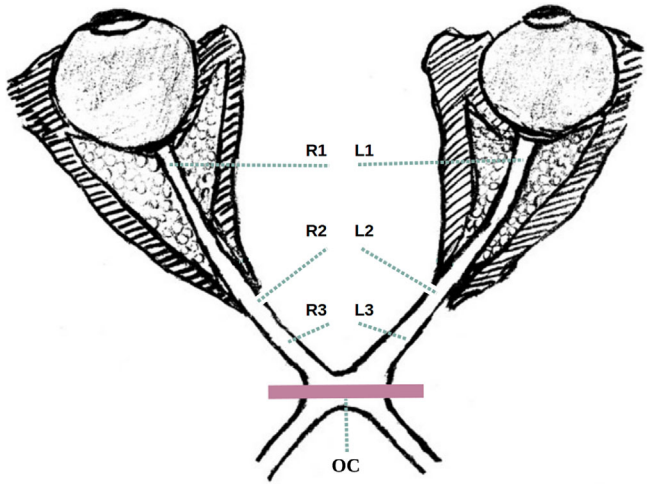

FIGURE 2 Schematic drawing of the optical nerve pathway in the transverse plane with both strands connecting one respective ocular globe with the optic chiasm (OC). Hatched areas representing osseous orbital structures, fat tissues are depicted as curls. On both strands, instructions required for landmark placement are pointed out by dotted green lines and numbered in descending order (R1-R3, L1-L3, OC). Viewing axis is inferior–superior (IS) by neuroradiological convention.

ROI placement, readers were instructed to first determine the OC and mark a single voxel in its isocenter. For both strands of the ON, three additional ROIs had to be marked in the same way with the following placement instructions: (1) at the optic disc, approximately 1 mm from the end of the ocular globe; (2) at the distal end of the optic canal; and (3) at halfway point between 2 and the initial ROI at the OC isocenter.

After spatial registration (see process description below), the spatial voxel information derived from all ROIs was converted into three-dimensional coordinates for use in the tractography algorithm. ROIs (1–3) on both strands were inflated into spheres with fixed radii (see below). The voxels in the OC isocenter were expanded to a flat rectangle to span an area of approximately 20 mm width by 7.5 mm height in the coronal plane to safely cover the standard human chiasm span (Puzniak et al., 2019; Salazar et al., 2018). We analyzed the inter-reader placement reliability to determine the level of difficulty of the different specific ROIs and the sequence type used in acquisition, respectively.

2.4 | Registration

We chose a registration strategy including VIBE images as the modifiable element and target DWI-variants to avoid ON alteration of the DWI datasets between preprocessing and FOD-generation. Linear registration was performed via 6- and 12-parameter (DOF) affine transformations (FLIRT) out of the FSL toolbox (Jenkinson et al., 2012). The relatively conservative 6-parameter DOF ('rigid body' = 3 rotations + 3 translations) is generally used to correct shifts and motions in intra-subject acquisitions, whilst 12-parameter DOF ('full-affine' = 'rigid body' + 3 scalings + 3 shears) may be more beneficial in compensating residual distortion in the target DWI volumes. The generated transformation matrices were extracted and consequently applied onto VIBE-drawn ROI-datasets, which were affected by the calculated transformations, respectively.

This resulted in eight combinations of DWI-FODs and ROIs: Each of the two DWI-variants (rs-/ss-EPI) with ROIs directly drawn onto the prepossessed DWI, as well as one VIBE-drawn nonregistered set for each DWI and additionally each VIBE transformed with 6- or 12-DOF, respectively.

2.5 | Tractography

Streamlines were generated via MRtrix3 (tckgen) using the probabilistic iFOD2 algorithm (Tournier et al., 2010). Thereby, the ROI closest to the ocular globes served as a seeding region, whereas the two remaining ROIs on each strand were mandatory includes. Each streamline terminates in the OC-ROI. Tractography parameters were fixed according to our preliminary experiments in tracking the ON (maximum angle 15 degree, step size = 0.5× voxel size, unidirectional). The radius of the seeding ROI was set at 2.5 mm with a seeding cutoff value of 0.08. Both other spherical ROIs were bilaterally set to a radius of 3 mm to safely cover the assumed ON thickness according to the literature (4–6 mm) (Becker et al., 2010; Salazar et al., 2018). The cutoff value for each tracking task was set at 0.05. In-depth explanation into tracking parameters can be found in the MRtrix3 user documentation (https://mrtrix.readthedocs.io).

The tracking task was limited to a maximal predefined number of 100,000 seeding points (streamline starting point candidates). Rather than defining a fixed number of streamlines, the limitation of seeding points is similar to a limitation of time, since the resources/capabilities (i.e., number of cores/threads) are known and consistent whilst being unbiased by computational performance fluctuations. Each tracking task stopped after successfully selecting 1000 streamlines (primary condition) or after utilization of all 100,000 seeds (secondary condition). Each task was run three times, and subsequently, streamline numbers were averaged. Completed tractograms of each image volume were checked for plausibility and potential deviations from expected ON anatomic pathways.

Noteworthy remark: The quantity of generated streamlines have little or no validity regarding biological assertions (Jones et al., 2013; Rheault et al., 2020) and were only used as an indicator of success with respect to ROI placement fidelity (between DWIs and VIBEs) and comparison of registration benefits (untransferred vs. transferred VIBE-ROI-datasets and VIBE-ROI transfer onto respective DWI sequences).

2.6 | Statistical analyses

Statistical analyses were performed using R (http://CRAN.R-project.org/; RStudio version 2022.07.2 Build 576) software packages. Statistical significance was defined for all analyses as an alpha level of 0.05.

Interreader reliability was estimated using intraclass correlation coefficient (ICC) and the 95% confident interval (CI). Interreader reliability was chosen as a single-rating, absolute-agreement, 2-way random-effects model (Koo & Li, 2016). Each image containing seven marked ROIs was converted into a set of separate three-dimensional coordinates per ROI. In turn, these were split into their x-, y- and z-components for ICC quantification and comparison among readers for each respective ROI/sequence combination. ICC-components were merged again for mean ICC calculation. Because of the small sample size, the lower 95% CI boundaries were chosen for comparison.

Classification followed the recommendations by Koo & Li, that is, values less than 0.5 are indicative of poor reliability, values between 0.5 and (up to) 0.75 indicate moderate reliability, values between 0.75 and (up to) 0.9 indicate good reliability and values greater than 0.90 indicate excellent reliability (Koo & Li, 2016).

3 | RESULTS

3.1 | ROI placement

Single ICC values for planar x-, y- and z-components and their means as well as 95% low CI boundaries are summarized in Table 1. Of 21 single-plane observations (Figure 3), ICC for VIBE resulted in 19 excellent and two good ratings, with no moderates or failures below 0.5 (rs-EPI: 7, excellent; 11, good; 3, moderate; 0, failures; ss-EPI: 12, excellent; 6, good; 3, moderate; 0, failures). Among the mean lower 95% boundary results, VIBE scored 11 as excellent (rs-EPI: 4; ss-EPI: 5), with further 5 as good results (rs-EPI: 5; ss-EPI: 8) and 2 as moderate (rs-EPI: 5 and 4 failed; ss-EPI: 2 and 3 failed).

3.2 | Tractography

In order to assess the results of the tracking task, the maximal (capped) selection of 1000 viable streamlines (within 100,000 seeding attempts) was set as 100%, whilst zero selected streamlines equaled a complete (0%) failure. We added a grading step at 5% (50 streamlines and above) for a more nuanced comparison. In each of the eight ROI/FOD-combinations, 120 tracking tasks were evaluated (each run three times and averaged): 20 subjects * 3 experts * 2 ON strands (left/right) = 120.

ROI placement directly drawn into rs-EPI resulted in 32 capped (26.7%) with 30 failures (25.0%), compared to 23 capped (19.2%) and 31 failures (25.8%) in ss-EPI-drawn ROIs. Further, rs-EPI passed the 5%-threshold in 51.7% of tasks (ss-EPI: 45.8%).

Between FODs, nonregistered VIBE-drawn ROIs capped 40 times (rs-EPI; 33.3%, 23 failures: 19.2%) compared to 33 (ss-EPI; 27.5%, 36 failures: 30.0%); 5%-threshold was 67.5% in rs-EPI compared to 55.0% in ss-EPI.

VIBE-drawn and subsequently registered ROI-sets capped on rs-EPI 39 times (32.5%, 16 failures: 13.3%) with 6-DOF and 41 times (34.2%, 16 failures: 13.3%) on 12-DOF. On ss-EPI FOD data, 6-DOF-registered ROIs capped 35 times (29.2%, 36 failures: 30.0%), whilst 12-DOF capped 34 times (28.3%, 34 failures: 28.3%). The threshold of 5% was exceeded in 70% (6-DOF) and 67.5% (12-DOF) of rs-EPI-FOD tasks. On ss-EPI-FODs, 55.0% (both 6-DOF and 12-DOF) of tasks surpassed the 5%-threshold.

In total, in all rs-EPI modalities combined, 5%-threshold was exceeded in 64.2% of tasks (31.7% capped, 17.7% failed), compared to 52.7% in all combined ss-EPI combinations (26.0% capped, 28.5% failed).

An explanatory overview of all results in relation to placement modalities and registration methods is shown in Figure 4.

4 | DISCUSSION

We examined DWI sequences in MR imaging of the optical nerve pathway to evaluate their suitability as targets for transferred ROI-datasets from structural images. Therefore, an rs-EPI sequence was compared to a standard ss-EPI sequence with respect to its presumed distortion resilience. A process overview is shown in Figure 5.

Prior to preprocessing and modelling of directional diffusion information (FOD-generation), highest reliability in interreader landmark placement on structural

TABLE 1 Single and mean intraclass correlation coefficient (ICC) values and respective 95% low ICC for x-, y- and z-coordinates oft each ROI position and the three acquisition types. Sorting of ROI landmarks is corresponding to anatomy with both ocular globes at the left/right and the optic chiasm in the middle (optic chiasm [OC], see Figure 2).

	Axis/ROI	R1	Low	R2	Low	R3	Low	OC	Low	L3	Low	L2	Low	L1	Low
rs-EPI	x	0.94	0.87	0.81	0.65	0.59	0.24	0.88	0.77	0.65	0.23	0.81	0.49	0.82	0.67
	y	0.88	0.75	0.81	0.63	0.82	0.63	0.65	0.41	0.83	0.63	0.82	0.62	0.89	0.76
	z	0.98	0.96	0.99	0.98	0.95	0.89	0.89	0.77	0.96	0.91	0.98	0.97	0.98	0.96
	Mean	0.93	0.86	0.87	0.75	0.79	0.59	0.80	0.65	0.81	0.59	0.87	0.69	0.90	0.79
ss-EPI	x	0.98	0.84	0.92	0.84	0.53	0.27	0.89	0.76	0.73	0.28	0.88	0.77	0.99	0.97
	y	0.95	0.93	0.89	0.79	0.87	0.74	0.61	0.35	0.89	0.79	0.92	0.83	0.98	0.91
	z	0.99	0.98	0.98	0.96	0.95	0.89	0.88	0.72	0.96	0.91	0.99	0.98	0.99	0.98
	Mean	0.97	0.92	0.93	0.86	0.78	0.63	0.79	0.61	0.86	0.66	0.93	0.86	0.99	0.95
VIBE	x	0.99	0.95	0.92	0.82	0.84	0.63	0.97	0.93	0.89	0.73	0.95	0.89	0.99	0.97
	y	0.98	0.90	0.96	0.89	0.95	0.88	0.99	0.97	1.00	0.88	0.97	0.94	0.98	0.81
	z	1.00	0.99	1.00	1.00	1.00	0.99	1.00	1.00	1.00	0.99	1.00	0.99	1.00	0.99
	Mean	0.99	0.95	0.96	0.90	0.93	0.84	0.98	0.97	0.96	0.87	0.97	0.94	0.99	0.93

Abbreviations: rs-EPI, readout-segmented EPI; ss-EPI, single-shot EPI.

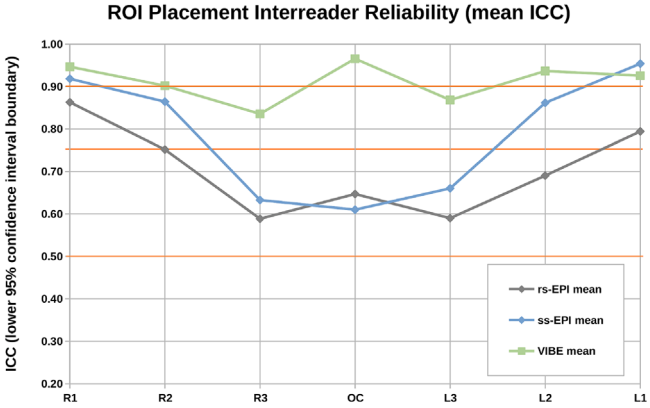

FIGURE 3 Lower 95% ICC confidence interval boundaries grouped for all datasets depending on imaging type. Sorting of ROI landmarks is corresponding to anatomy, optical nerve heads at the outer edges and the optic chiasm in the middle. Orange lines represent ICC classification delimiters after Koo & Li: values less than 0.5 are indicative of poor reliability, values between 0.5 and (up to) 0.75 indicate moderate reliability, values between 0.75 and (up to) 0.9 indicate good reliability, and values greater than 0.90 indicate excellent reliability.

images over both DWI-variants was demonstrated, and ROI-datasets were further subjected to our analysis. We respectively registered the data onto rs- and ss-EPI target volumes utilizing rigid body registration (6-DOF) and full-affine approaches (12-DOF). Qualitatively higher FOD-generation in the ON pathway is presumed by results from the subsequent tracking task performance with superior performance of rs-EPIs (67.5% to 70.0% over ss-EPIs with 55.0%).

Reviewing intra-variant registration differences, we found 12-DOF full-affine registration not performing significantly better or worse compared with 6-DOF in ss-EPI and in rs-EPI volumes.

Our results demonstrate a continuous advantage towards rs-EPI utilization as ROI landmarks in ON tractography. This is primarily verified by a more effective streamline selection performance, which indicates higher target suitability for structurally placed landmark information on rs-EPI compared to the established ss-EPI.

4.1 | ROI placement

During placement, the confidence of the readers' own accuracy was evaluated. In both DWI-variants, placement confidence of intercranial ROIs (3) and to a lesser degree canal ROIs (2), due to no or unclear anatomic landmarks, was assessed as low, whereas only few chiasm ROI (OC) and ROI (1) placements were deemed difficult. The placement for some rs-EPI volumes were considered as highly uncertain, particularly in the ocular globe region due to perceived blurring. On all VIBE images, placement of ROIs according to requirements was considered very easy with a high confidence into accuracy. This is in line with the ICC, as VIBE clearly outperformed both DWI sets in ROI (3) and the OC. In between DWI-variants, ss-EPI-drawn ROIs were placed with higher ICC reliability at both ocular globes and intercanal landmarks.

Distortion correction appeared to affect rs-EPI volumes stronger, with a higher perceived overlay match (after rigid body registration) between VIBEs and their

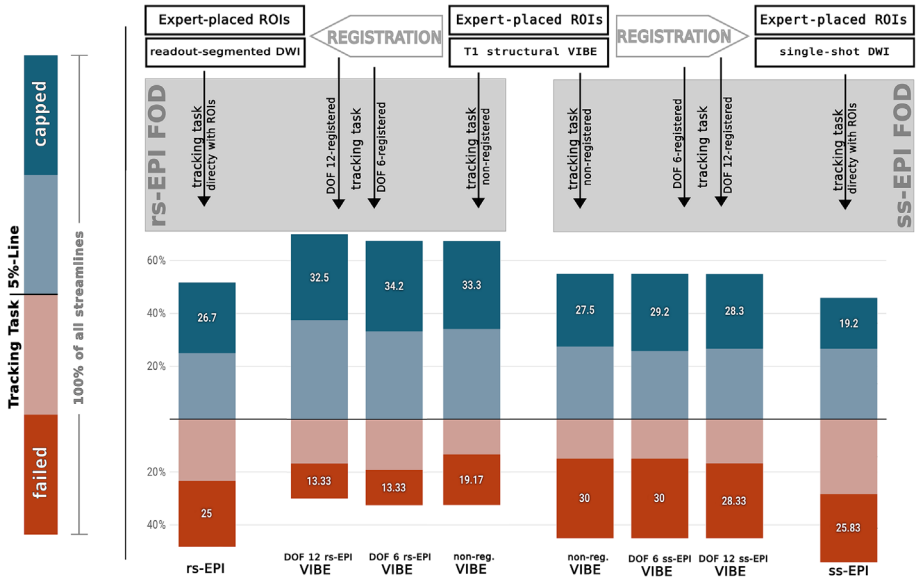

FIGURE 4 Depiction of tracking task results among all combinations of expert-placed regions of interest (ROIs) and registration methods. Results are shown as vertical 100%-bars (key on the left side) in relation to found streamlines in each tracking task. Data is centred around the 5%-success threshold (equaling 50 found streamlines). Proportions of capped (1000 streamlines found) and failed (0 streamlines found) results are marked in darker blue/red with according percentage shown.

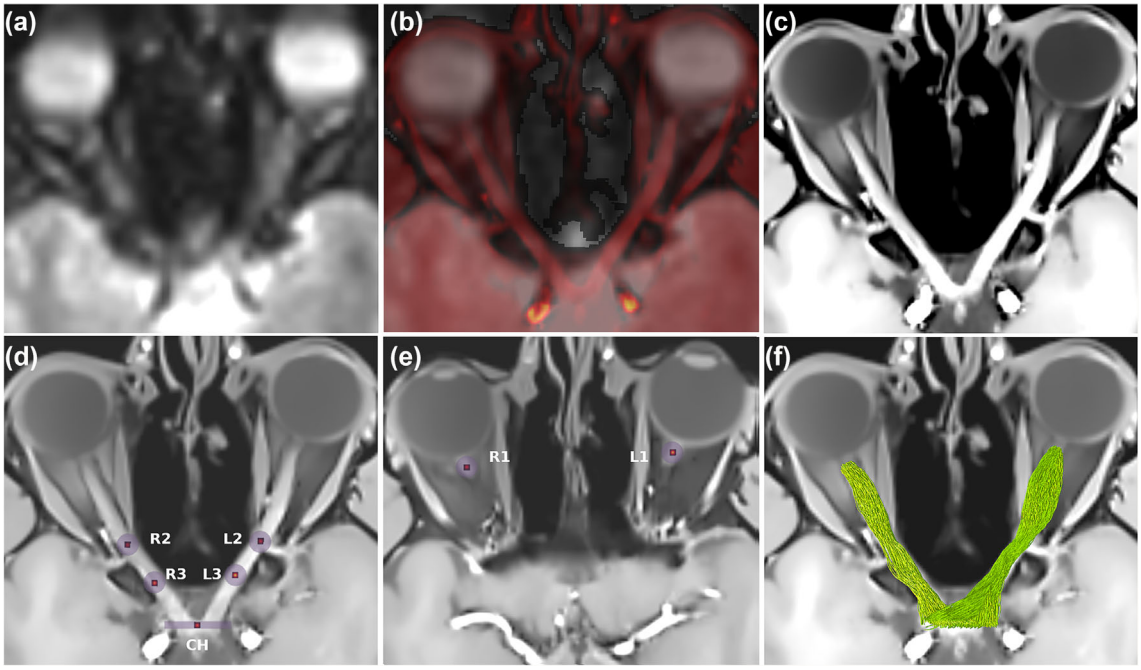

FIGURE 5 Illustration of registration and regions of interest (ROI) placement steps, shown are readout-segmented EPI (rs-EPI) and VIBE volumes of participant 03:(a) rs-EPI diffusion-weighted magnetic resonance imaging (DWI) image after preprocessing, depiction of contrast/saturation adjusted b0 image. (b) Overlay of target image A and C after registration of the latter. (c) Preprocessed and unregistered VIBE image. At this point, ROI landmarks are placed on VIBE and both DWI volumes. (d/e) show registered (here 6-degrees of freedom [DOF]) VIBE images with registration-shifted ROIs (red dots indicate initial placement) and their effective radii (violet). Both ocular ROIs shown separately in E due to the optic nerves curvature. (f) Depiction of successful tractograms in both strands, with all respective ROIs as mandatory inclusion areas.

rs-EPI targets. This also resulted in a stronger blurring in regions that were apparently strongest affected by the correction (ocular globes, intercranial region, OC) resulting in an offset of placement reliability due to less perceptible image contrast. Notably, this is in contrast to the reported overall blur reduction in the brain (Morelli et al., 2013; Wu & Miller, 2017).

Our results advocate for stepping away from ROIs drawn on diffusion-weighted images with low resolution and unclear anatomical referencing points. Especially,

due to the prevalence of misinterpretable surrounding data (Schilling et al., 2021), a high precision and reliability in all tractographic approaches in intercranial ON and OC regions are of utmost importance. In addition, this is of high relevance in the aforementioned approach of template-confined global tractography with subsequent ROI-based post-filtering, as the method is applied similarly.

4.2 | Acquisition

In DWI acquisition, factors determining the resolution of diffusion-derived data (e.g., FODs in CSD) and acquisition time must be balanced out (Runge et al., 2017). The latter are detrimental in all MR imaging by giving rise to motion artifacts that increasingly condense in low spatial resolution imaging such as DWI (Wu & Miller, 2017). Resolution factors depend on the chosen sequences (e.g., EPI variants) and on a combination of b-values with the encoding gradient directions. Our values (b = 800/1600 with 30 directions each) do not meet the gold standard (i.e., high-angular-resolution diffusion-weighted imaging (*HARDI*) recommendations (Tournier et al., 2019)) but are still deemed as minimally required for reliable FOD/fixel-based analysis (FBA) (Dhollander et al., 2021). Beneficially, this allows further comparison with available patient DWI data and more importantly implementation into routine workflows (acquisition times <10 min).

4.3 | Subject factors

Considering gaze behaviour during acquisition, we opted for an 'open but relaxed' instruction with an additional focus point, according to research recommendations discouraging fully closed eyes (Hoch et al., 2017). Detrimental correlations concerning the impact of eye movement on DWI parameters have been reported (Moodley et al., 2014). To our best knowledge, further insight into application on tractography does not exist; however, this is of relevance in clinical settings where noncooperative or illness-impaired patients are examined.

Interestingly, preliminary examinations regarding implants and retainers assumed only limited and locally confined influence, and thus, subjects with implants or retainers were not excluded. We did not find a correlation between failed FOD-generation/tracking and retainer presence. However, a high level of uncertainty regarding artifact causes has been reported, depending on material and field strength (Roser et al., 2021; Shalish et al., 2015), with extreme artifact radii in phantoms of up to 51 mm (Blankenstein et al., 2015). To our knowledge, no dedicated studies concerning retainer influence on diffusion-weighted imaging exist so far.

4.4 | Tractography

In most settings, pure streamline count is not sufficient as a measurement criteria, especially so in terms of connection strength (Jones et al., 2013; Le Bihan et al., 2006). We explicitly refrain from conclusions based on streamline numbers other than in our experimental comparison context described.

Having no universally valid cutoff-value reference for our iFOD2 algorithm, we used the historical lower algorithmic default boundary (0.05), following recommendations of MRtrix3 developers and operators, who advised against fixed values in favour of trials and best practices for varying purposes and application areas. Incidentally, we found consistent reporting of cutoff values to be lacking across a number of tractography-related publications.

We chose a predefined tracking task in order to compare small changes intra- and inter-DWI-variants of ROI/FOD-combinations. Inter-variant analysis showed clear performance advantages of all rs-EPI-based variants with 5%-threshold success of up to 70% over 55.0% in all ss-EPI-based combinations. Intra-variant analysis only saw noteworthy differences in rs-EPI 6-DOF-registered ROI-datasets, which outperformed nonregistered ROIs (67.5%) by 2.5%. Besides this, ROIs directly drawn on their respective DWI volumes performed worse in both variants (rs-EPI: 51.7%; ss-EPI: 45.8%) compared to all registered combinations.

During closer visual inspection into the lowest streamline count subjects, we have observed weak streamline selection performance and failures due to FOD shifts or presumed artifact build-up. This primarily affected the perceived position of the OC and papilla regions, with shifting beyond expectable anatomic assumptions and not traceable for human experts on the provided DWI volumes. For future research, automated approaches with combined, atlas-based (on structural images) and tractography-informed (on DWI) segmentation of ROIs might prove superior to prior concepts.

4.5 | Limitations and future developments

Due to small subject numbers, the significance of our results is limited. However, as comparable studies used similar numbers, we consider our work as a proof of methodical concept.

4.5.1 | Accelerated sequences

A promising way to mitigate time detriments from rs-EPI sequences is the use of simultaneous multi-slice (SMS) rs-EPI (Frost et al., 2015; Setsompop et al., 2012, 2015). In global brain applications, SMS-rs-EPI was found to achieve similar results regarding quality to rs-EPI but with a reduced acquisition time up to a factor of 3 (Ho et al., 2018; Manoliu et al., 2017; Runge et al., 2017). Hence, a reduction in acquisition time has the benefit of reduced motion artifacts or, alternatively, time may be reinvested for the benefit of higher b-values and more gradient directions to approach HARDI requirements, with an optimal balance yet to be determined.

4.5.2 | Fixel-based-analysis

The FBA framework (Raffelt et al., 2017) provides advanced derivable DWI metrics which fulfil the requirements for quantitative analysis. Previous studies on FBA showed promising results in a variety of observation areas (Dhollander et al., 2021) with some demonstrating pathological changes in ON morphology and functionality (Haykal et al., 2020). Availability and application of templates is mandatory in group study designs such as FBA and hence one of the key drivers behind this study.

4.5.3 | Outlook

Based on our results, we will focus on template development as our next step. Further standardized and established tractographic methods of ON and complete visual system depiction and analysis may be applied in early detection of ON deterioration processes and even in routine screenings of vulnerable demographic groups (e.g., the presence of illness in the family, age, ethnicity) (Miller et al., 2019; Nuzzi et al., 2018; Weinreb et al., 2014).

5 | CONCLUSION

We compared expert-placed ROI-data transfer from structural T1-weighted volumes onto standard EPI sequence for DWI acquisition to an advanced, rs-EPI sequence for their performance in a predefined targeted tracking task in the ON. Preprocessed rs-EPI volumes confirmed distortion resilience as well as higher reliability in successful modelling of directional diffusion information. In combination with appropriate preprocessing and registration strategies, rs-EPI is more suitable for transferred ROI-data from structural images compared to the ss-EPI standard DWI. Based on these findings, this approach may be applied in the development of WM templates or used for further group studies and quantitative analysis methods.

AUTHOR CONTRIBUTIONS

Markus Janko: Conceptualization; data curation; formal analysis; investigation; methodology; software; writing—original draft. **Sascha D. Santaniello:** Data curation; software; writing—review and editing. **Carolin Brockmann:** Investigation; writing—review and editing. **Marcel Wolf:** Investigation; writing—review and editing. **Nils F. Grauhan:** Investigation; writing—review and editing. **Vanessa I. Schöffling:** Methodology; resources; writing—review and editing. **Violeta Dimova:** Formal analysis; supervision; writing—review and editing. **Katharina Ponto:** Writing—review and editing. **Esther M. Hoffmann:** Writing—review and editing. **Wolfgang Kleinekofort:** Conceptualization; supervision; writing—review and editing. **Ahmed E. Othman:** Conceptualization; funding acquisition; project administration; writing—review and editing. **Marc A. Brockmann:** Conceptualization; funding acquisition; project administration; writing—review and editing. **Andrea Kronfeld:** Conceptualization; investigation; methodology; project administration; resources; supervision; writing—review and editing.

CONFLICT OF INTEREST STATEMENT

All authors declare that they have no conflicts of interest.

PEER REVIEW

The peer review history for this article is available at https://www.webofscience.com/api/gateway/wos/peer-review/10.1111/ejn.16490.

DATA AVAILABILITY STATEMENT

The data that support the findings of this study are available from the corresponding author upon reasonable request.

CLINICAL TRIAL REGISTRATION

DRKS00023278.

ORCID

Markus Janko https://orcid.org/0000-0002-6123-0518

REFERENCES

Allen, B., Schmitt, M. A., Kushner, B. J., & Rokers, B. (2018). Retinothalamic white matter abnormalities in amblyopia. *Investigative Ophthalmology & Visual Science*, *59*(2), 921–929. https://doi.org/10.1167/iovs.17-22930

Altıntaş, Ö., Gümüştaş, S., Cinik, R., Anık, Y., Özkan, B., & Karabaş, L. (2017). Correlation of the measurements of optical coherence tomography and diffuse tension imaging of optic pathways in amblyopia. *International Ophthalmology*, *37*(1), 85–93. https://doi.org/10.1007/s10792-016-0229-0

Andersson, J. L. R., Skare, S., & Ashburner, J. (2003). How to correct susceptibility distortions in spin-echo echo-planar images: Application to diffusion tensor imaging. *NeuroImage*, *20*(2), 870–888. https://doi.org/10.1016/S1053-8119(03)00336-7

Andersson, J. L. R., & Sotiropoulos, S. N. (2016). An integrated approach to correction for off-resonance effects and subject movement in diffusion MR imaging. *NeuroImage*, *125*, 1063–1078. https://doi.org/10.1016/j.neuroimage.2015.10.019

Archer, D. B., Vaillancourt, D. E., & Coombes, S. A. (2018). A template and probabilistic atlas of the human sensorimotor tracts using diffusion MRI. *Cerebral Cortex*, *28*(5), 1685–1699. https://doi.org/10.1093/cercor/bhx066

Avants, B. B., Tustison, N., & Johnson, H. (2014). Advanced Normalization Tools (ANTS). http://stnava.github.io/ANTs/

Basser, P. J., Pajevic, S., Pierpaoli, C., Duda, J., & Aldroubi, A. (2000). In vivo fiber tractography using DT-MRI data. *Magnetic Resonance in Medicine*, *44*(4), 625–632. https://doi.org/10.1002/1522-2594(200010)44:4<625::aid-mrm17>3.0.co;2-o

Becker, D., Scherer, M., Neher, P., Jungk, C., Jesser, J., Pflüger, I., Brinster, R., Bendszus, M., Bruckner, T., Maier-Hein, K., & Unterberg, A. (2020). Going beyond diffusion tensor imaging tractography in eloquent glioma surgery–high-resolution fiber tractography: Q-ball or constrained spherical deconvolution? *World Neurosurgery*, *134*, e596–e609. https://doi.org/10.1016/j.wneu.2019.10.138

Becker, M., Masterson, K., Delavelle, J., Viallon, M., Vargas, M.-I., & Becker, C. D. (2010). Imaging of the optic nerve. *European Journal of Radiology*, *74*(2), 299–313. https://doi.org/10.1016/j.ejrad.2009.09.029

Blankenstein, F., Truong, B. T., Thomas, A., Thieme, N., & Zachriat, C. (2015). Zur Vorhersagbarkeit von Suszeptibilitätsartefakten durch metallische orthodontische Apparaturen in der Magnetresonanztomographie. *Journal of Orofacial Orthopedics/Fortschritte der Kieferorthopädie*, *76*(1), 14–29. https://doi.org/10.1007/s00056-014-0258-0

Brockmann, M. A., & Elflein, H. M. (2019). Neuroradiology in ophthalmology. *Der Ophthalmologe: Zeitschrift Der Deutschen Ophthalmologischen Gesellschaft*, *116*(7), 689–706. https://doi.org/10.1007/s00347-019-0922-2

Chen, D. Q., Dell'Acqua, F., Rokem, A., Garyfallidis, E., Hayes, D. J., Zhong, J., & Hodaie, M. (2019). Diffusion Weighted Image Co-registration: Investigation of Best Practices (p. 864108). https://doi.org/10.1101/864108

Chow, L. S., & Paley, M. N. J. (2021). Recent advances on optic nerve magnetic resonance imaging and post-processing. *Magnetic Resonance Imaging*, *79*, 76–84. https://doi.org/10.1016/j.mri.2021.03.014

Christiaens, D., Reisert, M., Dhollander, T., Sunaert, S., Suetens, P., & Maes, F. (2015). Global tractography of multi-shell diffusion-weighted imaging data using a multi-tissue model. *NeuroImage*, *123*, 89–101. https://doi.org/10.1016/j.neuroimage.2015.08.008

Dhollander, T., Clemente, A., Singh, M., Boonstra, F., Civier, O., Duque, J. D., Egorova, N., Enticott, P., Fuelscher, I., Gajamange, S., Genc, S., Gottlieb, E., Hyde, C., Imms, P., Kelly, C., Kirkovski, M., Kolbe, S., Liang, X., Malhotra, A., … Caeyenberghs, K. (2021). Fixel-based analysis of diffusion MRI: Methods, applications, challenges and opportunities. *NeuroImage*, *241*, 118417. https://doi.org/10.1016/j.neuroimage.2021.118417

Frost, R., Jezzard, P., Douaud, G., Clare, S., Porter, D. A., & Miller, K. L. (2015). Scan time reduction for readout-segmented EPI using simultaneous multislice acceleration: Diffusion-weighted imaging at 3 and 7 tesla: Blipped-CAIPI rs-EPI. *Magnetic Resonance in Medicine*, *74*(1), 136–149. https://doi.org/10.1002/mrm.25391

Golby, A. J., Kindlmann, G., Norton, I., Yarmarkovich, A., Pieper, S., & Kikinis, R. (2011). Interactive diffusion tensor tractography visualization for neurosurgical planning. *Neurosurgery*, *68*(2), 496–505. https://doi.org/10.1227/NEU.0b013e3182061ebb

Hakulinen, U., Brander, A., Ryymin, P., Öhman, J., Soimakallio, S., Helminen, M., Dastidar, P., & Eskola, H. (2012). Repeatability and variation of region-of-interest methods using quantitative diffusion tensor MR imaging of the brain. *BMC Medical Imaging*, *12*(1), 30. https://doi.org/10.1186/1471-2342-12-30

Haykal, S., Jansonius, N. M., & Cornelissen, F. W. (2020). Investigating changes in axonal density and morphology of glaucomatous optic nerves using fixel-based analysis. *European Journal of Radiology*, *133*, 109356. https://doi.org/10.1016/j.ejrad.2020.109356

He, J., Zhang, F., Xie, G., Yao, S., Feng, Y., Bastos, D. C. A., Rathi, Y., Makris, N., Kikinis, R., Golby, A. J., & O'Donnell, L. J. (2020). Comparison of multiple tractography methods for reconstruction of the retinogeniculate visual pathway using diffusion MRI [preprint]. *Neuroscience*, *42*(12), 3887–3904. https://doi.org/10.1101/2020.09.19.304758

Ho, M., Becker, A., Ulbrich, E., Manoliu, A., Kuhn, F. P., Eberhard, M., & Filli, L. (2018). Comparison of simultaneous multi-slice readout-segmented EPI and conventional single-shot EPI for diffusion tensor imaging of the ulnar nerve. *Heliyon*, *4*(10), e00853. https://doi.org/10.1016/j.heliyon.2018.e00853

Hoch, M. J., Bruno, M. T., & Shepherd, T. M. (2017). Advanced MRI of the optic nerve. *Journal of Neuro-Ophthalmology*, *37*(2), 187–196. https://doi.org/10.1097/WNO.0000000000000511

Jacquesson, T., Cotton, F., Attyé, A., Zaouche, S., Tringali, S., Bosc, J., Robinson, P., Jouanneau, E., & Frindel, C. (2019). Probabilistic tractography to predict the position of cranial nerves displaced by skull base tumors: Value for surgical strategy through a case series of 62 patients. *Neurosurgery*, *85*(1), E125–E136. https://doi.org/10.1093/neuros/nyy538

Jenkinson, M., Beckmann, C. F., Behrens, T. E. J., Woolrich, M. W., & Smith, S. M. (2012). FSL. *NeuroImage*, *62*(2), 782–790. https://doi.org/10.1016/j.neuroimage.2011.09.015

Jones, D. K., Knösche, T. R., & Turner, R. (2013). White matter integrity, fiber count, and other fallacies: The do's and don'ts of diffusion MRI. *NeuroImage*, *73*, 239–254. https://doi.org/10.1016/j.neuroimage.2012.06.081

Koo, T. K., & Li, M. Y. (2016). A guideline of selecting and reporting Intraclass correlation coefficients for reliability research.

Journal of Chiropractic Medicine, *15*(2), 155–163. https://doi.org/10.1016/j.jcm.2016.02.012

Koyasu, S., Iima, M., Umeoka, S., Morisawa, N., Porter, D. A., Ito, J., Le Bihan, D., & Togashi, K. (2014). The clinical utility of reduced-distortion readout-segmented echo-planar imaging in the head and neck region: Initial experience. *European Radiology*, *24*(12), 3088–3096. https://doi.org/10.1007/s00330-014-3369-5

Le Bihan, D., & Breton, E. (1985). In vivo magnetic resonance imaging of diffusion. *Comptes Rendus Des Seances de l'Academie Des Sciences*. Serie 2, *301*(15), 1109–1112.

Le Bihan, D., Poupon, C., Amadon, A., & Lethimonnier, F. (2006). Artifacts and pitfalls in diffusion MRI. *Journal of Magnetic Resonance Imaging: JMRI*, *24*(3), 478–488. https://doi.org/10.1002/jmri.20683

Mangin, J.-F., Fillard, P., Cointepas, Y., Le Bihan, D., Frouin, V., & Poupon, C. (2013). Toward global tractography. *NeuroImage*, *80*, 290–296. https://doi.org/10.1016/j.neuroimage.2013.04.009

Manoliu, A., Ho, M., Piccirelli, M., Nanz, D., Filli, L., Dappa, E., Liu, W., Ettlin, D. A., Boss, A., Andreisek, G., & Kuhn, F. P. (2017). Simultaneous multislice readout-segmented echo planar imaging for accelerated diffusion tensor imaging of the mandibular nerve: A feasibility study: SMS rs-EPI for accelerated DTI. *Journal of Magnetic Resonance Imaging*, *46*(3), 663–677. https://doi.org/10.1002/jmri.25603

Miller, N., Liu, Y., Krivochenitser, R., & Rokers, B. (2019). Linking neural and clinical measures of glaucoma with diffusion magnetic resonance imaging (dMRI). *PLoS ONE*, *14*(5), e0217011. https://doi.org/10.1371/journal.pone.0217011

Moodley, A., Rae, W. I. D., Brijmohan, Y., Durand, M., Connolly, C., Michowicz, A., & Bhigjee, A. (2014). The impact of optic nerve movement on optic nerve magnetic resonance diffusion parameters. *South African Journal of Radiology*, *18*(1), 1–5 https://doi.org/10.4102/sajr.v18i1.596

Morelli, J., Porter, D., Ai, F., Gerdes, C., Saettele, M., Feiweier, T., Padua, A., Dix, J., Marra, M., Rangaswamy, R., & Runge, V. (2013). Clinical evaluation of single-shot and readout-segmented diffusion-weighted imaging in stroke patients at 3 T. *Acta Radiologica*, *54*(3), 299–306. https://doi.org/10.1258/ar.2012.120541

Mori, S., & Zhang, J. (2006). Principles of diffusion tensor imaging and its applications to basic neuroscience research. *Neuron*, *51*(5), 527–539. https://doi.org/10.1016/j.neuron.2006.08.012

Nucifora, P. G. P., Verma, R., Lee, S.-K., & Melhem, E. R. (2007). Diffusion-tensor MR imaging and tractography: Exploring brain microstructure and connectivity. *Radiology*, *245*(2), 367–384. https://doi.org/10.1148/radiol.2452060445

Nuzzi, R., Dallorto, L., & Rolle, T. (2018). Changes of visual pathway and brain connectivity in glaucoma: A systematic review. *Frontiers in Neuroscience*, *12*, 363. https://doi.org/10.3389/fnins.2018.00363

Porter, D. A., & Heidemann, R. M. (2009). High resolution diffusion-weighted imaging using readout-segmented echo-planar imaging, parallel imaging and a two-dimensional navigator-based reacquisition: EPI with parallel imaging and 2D reacquisition. *Magnetic Resonance in Medicine*, *62*(2), 468–475. https://doi.org/10.1002/mrm.22024

Puzniak, R. J., Ahmadi, K., Kaufmann, J., Gouws, A., Morland, A. B., Pestilli, F., & Hoffmann, M. B. (2019). Quantifying nerve decussation abnormalities in the optic chiasm. *NeuroImage Clinical*, *24*, 102055. https://doi.org/10.1016/j.nicl.2019.102055

Raffelt, D. A., Tournier, J.-D., Smith, R. E., Vaughan, D. N., Jackson, G., Ridgway, G. R., & Connelly, A. (2017). Investigating white matter fibre density and morphology using fixel-based analysis. *NeuroImage*, *144*, 58–73. https://doi.org/10.1016/j.neuroimage.2016.09.029

Rheault, F., Poulin, P., Caron, A. V., St-Onge, E., & Descoteaux, M. (2020). Common misconceptions, hidden biases and modern challenges of dMRI tractography. *Journal of Neural Engineering*, *17*(1), 011001. https://doi.org/10.1088/1741-2552/ab6aad

Riffert, T. W., Schreiber, J., Anwander, A., & Knösche, T. R. (2014). Beyond fractional anisotropy: Extraction of bundle-specific structural metrics from crossing fiber models. *NeuroImage*, *100*, 176–191. https://doi.org/10.1016/j.neuroimage.2014.06.015

Rofsky, N. M., Lee, V. S., Laub, G., Pollack, M. A., Krinsky, G. A., Thomasson, D., Ambrosino, M. M., & Weinreb, J. C. (1999). Abdominal MR imaging with a volumetric interpolated breath-hold examination. *Radiology*, *212*(3), 876–884. https://doi.org/10.1148/radiology.212.3.r99se34876

Roser, C., Hilgenfeld, T., Sen, S., Badrow, T., Zingler, S., Heiland, S., Bendszus, M., Lux, C. J., & Juerchott, A. (2021). Evaluation of magnetic resonance imaging artifacts caused by fixed orthodontic CAD/CAM retainers—An in vitro study. *Clinical Oral Investigations*, *25*(3), 1423–1431. https://doi.org/10.1007/s00784-020-03450-x

Runge, V. M., Richter, J. K., & Heverhagen, J. T. (2017). Speed in clinical magnetic resonance. *Investigative Radiology*, *52*(1), 1–17. https://doi.org/10.1097/RLI.0000000000000330

Salazar, J. J., Ramírez, A. I., Hoz, R. D., Salobrar-Garcia, E., Rojas, P., Fernández-Albarral, J. A., López-Cuenca, I., Rojas, B., Triviño, A., & Ramírez, J. M. (2018). Anatomy of the human optic nerve: Structure and function. In *Optic nerve*. IntechOpen. https://doi.org/10.5772/intechopen.79827

Schilling, K. G., Tax, C. M. W., Rheault, F., Landman, B., Anderson, A., Descoteaux, M., & Petit, L. (2021). Prevalence of white matter pathways coming into a single diffusion MRI voxel orientation: The bottleneck issue in tractography [preprint]. *Neuroscience*, 2021-06 https://doi.org/10.1101/2021.06.22.449454

Scilpy. (2021). [Python]. Sherbrooke Connectivity Imaging Lab. https://github.com/scilus/scilpy (Original work published 2015)

Setsompop, K., Cauley, S. F., & Wald, L. L. (2015). Advancing Diffusion MRI Using Simultaneous Multi-Slice Echo Planar Imaging.

Setsompop, K., Cohen-Adad, J., Gagoski, B. A., Raij, T., Yendiki, A., Keil, B., Wedeen, V. J., & Wald, L. L. (2012). Improving diffusion MRI using simultaneous multi-slice echo planar imaging. *NeuroImage*, *63*(1), 569–580. https://doi.org/10.1016/j.neuroimage.2012.06.033

Shalish, M., Dykstein, N., Friedlander-Barenboim, S., Ben-David, E., Gomori, J. M., & Chaushu, S. (2015). Influence of common fixed retainers on the diagnostic quality of cranial magnetic resonance images. *American Journal of Orthodontics and Dentofacial Orthopedics*, *147*(5), 604–609. https://doi.org/10.1016/j.ajodo.2014.11.022

Sims, J. R., Chen, A. M., Sun, Z., Deng, W., Colwell, N. A., Colbert, M. K., Zhu, J., Sainulabdeen, A., Faiq, M. A., Bang, J. W., & Chan, K. C. (2020). Role of structural, metabolic, and functional MRI in monitoring visual system impairment and recovery. *Journal of Magnetic Resonance Imaging: JMRI*, *54*, 1706–1729. https://doi.org/10.1002/jmri.27367

Sotiropoulos, S. N., Jbabdi, S., Xu, J., Andersson, J. L., Moeller, S., Auerbach, E. J., Glasser, M. F., Hernandez, M., Sapiro, G., Jenkinson, M., Feinberg, D. A., Yacoub, E., Lenglet, C., Van Essen, D. C., Ugurbil, K., & Behrens, T. E. J. (2013). Advances in diffusion MRI acquisition and processing in the human connectome project. *NeuroImage*, *80*, 125–143. https://doi.org/10.1016/j.neuroimage.2013.05.057

Suarez, R. O., Commowick, O., Prabhu, S. P., & Warfield, S. K. (2012). Automated delineation of white matter fiber tracts with a multiple region-of-interest approach. *NeuroImage*, *59*(4), 3690–3700. https://doi.org/10.1016/j.neuroimage.2011.11.043

Theaud, G., Houde, J.-C., Boré, A., Rheault, F., Morency, F., & Descoteaux, M. (2020). TractoFlow: A robust, efficient and reproducible diffusion MRI pipeline leveraging nextflow & singularity. *NeuroImage*, *218*, 116889. https://doi.org/10.1016/j.neuroimage.2020.116889

Tournier, J.-D., Calamante, F., & Connelly, A. (2010). Improved probabilistic streamlines tractography by 2nd order integration over fibre orientation distributions. *Proceedings of the International Society for Magnetic Resonance in Medicine*. (ISMRM), 18.

Tournier, J.-D., Calamante, F., & Connelly, A. (2013). Determination of the appropriate b value and number of gradient directions for high-angular-resolution diffusion-weighted imaging. *NMR in Biomedicine*, *26*(12), 1775–1786. https://doi.org/10.1002/nbm.3017

Tournier, J.-D., Calamante, F., Gadian, D. G., & Connelly, A. (2004). Direct estimation of the fiber orientation density function from diffusion-weighted MRI data using spherical deconvolution. *NeuroImage*, *23*(3), 1176–1185. https://doi.org/10.1016/j.neuroimage.2004.07.037

Tournier, J.-D., Smith, R., Raffelt, D., Tabbara, R., Dhollander, T., Pietsch, M., Christiaens, D., Jeurissen, B., Yeh, C.-H., & Connelly, A. (2019). MRtrix3: A fast, flexible and open software framework for medical image processing and visualisation. *NeuroImage*, *202*, 116137. https://doi.org/10.1016/j.neuroimage.2019.116137

Tournier, J.-D., Yeh, C.-H., Calamante, F., Cho, K.-H., Connelly, A., & Lin, C.-P. (2008). Resolving crossing fibres using constrained spherical deconvolution: Validation using diffusion-weighted imaging phantom data. *NeuroImage*, *42*(2), 617–625. https://doi.org/10.1016/j.neuroimage.2008.05.002

Wan, H., Sha, Y., Zhang, F., Hong, R., Tian, G., & Fan, H. (2016). Diffusion-weighted imaging using readout-segmented echo-planar imaging, parallel imaging, and two-dimensional navigator-based reacquisition in detecting acute optic neuritis. *Journal of Magnetic Resonance Imaging*, *43*(3), 655–660. https://doi.org/10.1002/jmri.25026

Weinreb, R. N., Aung, T., & Medeiros, F. A. (2014). The pathophysiology and treatment of glaucoma: A review. *JAMA*, *311*(18), 1901–1911. https://doi.org/10.1001/jama.2014.3192

Wetzel, S. G., Johnson, G., Tan, A. G. S., Cha, S., Knopp, E. A., Lee, V. S., Thomasson, D., & Rofsky, N. M. (2002). Three-dimensional, T1-weighted gradient-echo imaging of the brain with a volumetric interpolated examination. *AJNR: American Journal of Neuroradiology*, *23*(6), 995–1002.

Wu, C.-N. (2019). Assessment of optic nerve and optic tract alterations in patients with orbital space-occupying lesions using probabilistic diffusion tractography. *International Journal of Ophthalmology*, *12*(8), 1304–1310. https://doi.org/10.18240/ijo.2019.08.11

Wu, W., & Miller, K. L. (2017). Image formation in diffusion MRI: A review of recent technical developments. *Journal of Magnetic Resonance Imaging: JMRI*, *46*(3), 646–662. https://doi.org/10.1002/jmri.25664

Xu, X.-Q., Liu, J., Hu, H., Su, G.-Y., Zhang, Y.-D., Shi, H.-B., & Wu, F.-Y. (2016). Improve the image quality of orbital 3 T diffusion-weighted magnetic resonance imaging with readout-segmented echo-planar imaging. *Clinical Imaging*, *40*(4), 793–796. https://doi.org/10.1016/j.clinimag.2016.03.002

Yeom, K. W., Holdsworth, S. J., Van, A. T., Iv, M., Skare, S., Lober, R. M., & Bammer, R. (2013). Comparison of readout-segmented echo-planar imaging (EPI) and single-shot EPI in clinical application of diffusion-weighted imaging of the pediatric brain. *American Journal of Roentgenology*, *200*(5), W437–W443. https://doi.org/10.2214/AJR.12.9854

Zhou, F., Li, Q., Zhang, X., Ma, H., Zhang, G., Du, S., Zhang, L., Benkert, T., & Zhang, Z. (2022). Reproducibility and feasibility of optic nerve diffusion MRI techniques: Single-shot echo-planar imaging (EPI), readout-segmented EPI, and reduced field-of-view diffusion-weighted imaging. *BMC Medical Imaging*, *22*(1), 96. https://doi.org/10.1186/s12880-022-00814-5

SUPPORTING INFORMATION

Additional supporting information can be found online in the Supporting Information section at the end of this article.

How to cite this article: Janko, M., Santaniello, S. D., Brockmann, C., Wolf, M., Grauhan, N. F., Schöffling, V. I., Dimova, V., Ponto, K., Hoffmann, E. M., Kleinekofort, W., Othman, A. E., Brockmann, M. A., & Kronfeld, A. (2024). Comparison of T1-weighted landmark placement and ROI transfer onto diffusion-weighted EPI sequences for targeted tractography tasks in the optic nerve. *European Journal of Neuroscience*, *60*(5), 4987–4999. https://doi.org/10.1111/ejn.16490